Sound & Vibration 2026, 60(6), 4756.
doi: https://doi.org/10.59400/sv4756

Article

Interval type-2 fuzzy hydroelastic Ritz–Koopman optimization of a partially filled cylindrical tank for robust sloshing-induced vibro-acoustic suppression

Suleiman Ibrahim Mohammad[1], Yogeesh Nijalingappa[2,3,4,*], Seif Al Bustanji[5], Asokan Vasudevan[1], P. William[6,7], Chethana N. S.[8]

[1] Faculty of Business and Communications, INTI International University, Nilai 71800, Malaysia; dr_sliman73@aabu.edu.jo (SIM); asokan.vasudevan@newinti.edu.my (AV)
[2] Department of Mathematics & Natural Sciences, Gulf University for Science & Technology, Safat 13060, Kuwait
[3] Department of Mathematics, Government First Grade College, Tumkur 572102, India
[4] Research Fellow, INTI International University, Nilai 71800, Malaysia
[5] Faculty of Technical Education, Hourani Center for Applied Scientific Research (HCASR), Al-Ahliyya Amman University, Amman 19111, Jordan; s.albustanji@ammanu.edu.jo
[6] School of Computer Science and Technology, Karunya Institute of Technology and Sciences (Deemed University), Coimbatore 641114, India; william160891@gmail.com
[7] Centre for Research and Consultancy, UNITAR International University, Petaling Jaya 47301, Malaysia
[8] Department of Mathematics, Central University of Karnataka, Kalaburagi 585367, India; hetanachetana100@gmail.com
*** Corresponding author:** Yogeesh Nijalingappa, yogeesh.n@ka.gov.in

CITATION

Mohammad SI, Nijalingappa Y, Al Bustanji S, et al. Interval type-2 fuzzy hydroelastic Ritz–Koopman optimization of a partially filled cylindrical tank for robust sloshing-induced vibro-acoustic suppression. Sound & Vibration. 2026; 60(6): 4756. https://doi.org/10.59400/sv4756

ARTICLE INFO

Received: 31 July 2026
Revised: 17 August 2026
Accepted: 21 August 2026
Available online: 2 September 2026

Abstract: Partially filled storage and transport tanks often radiate objectionable low-frequency sound because liquid sloshing, flexible shell modes, and uncertain damping interact in the same operating band. This paper develops a compact hydroelastic vibro-acoustic design method for a vertical cylindrical tank equipped with internal porous annular baffles and external viscoelastic rings. The fluid is represented by Bessel-based sloshing modes, the shell by a Ritz expansion, and the nonlinear free-surface contribution by a cubic Koopman–Galerkin lifting. Interval type-2 fuzzy sets describe epistemic uncertainty in fill height, fluid density, shell stiffness, loss factor, and baffle clogging. A deterministic design and a proposed fuzzy robust design are compared over alpha-plane uncertainty scenarios using peak sound power, band-averaged sound power, wall acceleration, and wave-height constraints. The proposed design reduces the 95th-percentile peak sound power from 57.84 dB in the uncontrolled tank to 48.55 dB, decreases the 95th-percentile band-averaged acoustic level from 28.47 dB to 26.73 dB, and lowers the 95th-percentile wall-acceleration level from 130.48 dB to 120.34 dB. Relative to the deterministic optimum, the robust design has a 0.216 dB higher nominal peak and a 0.173 dB higher 95th-percentile peak. Still, it lowers the 95th-percentile band mean by 1.059 dB and wall acceleration by 0.613 dB. The contribution is the integrated reduced-order design workflow; physical validation remains necessary.

Keywords: sound and vibration; hydroelasticity; sloshing; cylindrical tank; interval type-2 fuzzy sets; vibro-acoustic radiation; Koopman–Galerkin model; robust optimization

1. Introduction

Partially filled tanks appear in fuel transport, chemical processing, railway vehicles, offshore equipment, and seismic storage infrastructure. Their vibration behaviour is difficult to control because the dominant energy path is not a single structural resonance. A low-frequency free-surface wave generates time-dependent hydrodynamic pressure; the flexible cylindrical wall converts that pressure into shell vibration; and the vibrating wall radiates low-frequency sound into the surrounding air. Classical equivalent-spring sloshing models are valuable for global load estimation, while hydroelastic shell formulations are required when the wall flexibility is not negligible. Earlier studies established the foundations through classical tank dynamics and partially filled shell models [1–5], free-surface and hydroelastic formulations [6–10], baffled cylindrical sloshing [11–15], and recent elastic-baffle and viscosity effects [16–18]. However, the practical design problem still has two gaps. First, tank parameters are rarely crisp: fill height, shell stiffness, viscous losses, and baffle condition may vary from one operation to another. Second, a deterministic treatment may give a low nominal peak but a fragile response when damping or fill height moves away from its assumed value. Recent studies have examined elastic-baffle interaction, experimentally observed sloshing, viscosity-dependent damping, and coupled cylindrical configurations [16–19]. Related vibration analyses of porous microplates and stiffened cylindrical panels are reported by Liu et al. and Zhou et al. [20, 21], while scaled-tank experiments further demonstrate the dependence of resonant response on fill and excitation [22]. These works provide useful high-fidelity or experimental benchmarks, but they do not combine baffle-ring co-design, acoustic response, and interval type-2 epistemic propagation in one reduced-order optimization. The recent literature also shows why validation cannot rely on a single comparison quantity. Elastic-baffle studies commonly report free-surface elevation, pressure and baffle deformation, whereas shell-vibration studies emphasize natural frequencies and modal shapes. The present work therefore links elevation, wall response and acoustic power, but uses a lower-fidelity model than those in the benchmark studies. The comparison establishes a distinct design purpose rather than superiority over computational fluid dynamics (CFD) or experiments. It also motivates retaining the two reviewer-suggested vibration references, which provide current examples of higher-order kinematic assumptions and stiffened cylindrical-panel modelling relevant to the structural part of the formulation.

The present paper develops a high-order but compact computational method for robust vibro-acoustic suppression. The proposed system is a vertical cylindrical tank with porous annular baffles inside the liquid and viscoelastic rings outside the shell. The purpose is not to replace detailed computational fluid dynamics. Rather, the aim is to create a mathematically transparent design model that can be evaluated many times inside an uncertainty-aware optimizer. **Figure 1** shows the hydroelastic configuration, while **Table 1** lists the main physical quantities used in the formulation.

The contribution is the integrated coupling of a Bessel-Ritz hydroelastic state, cubic correction, interval type-2 uncertainty propagation and baffle-ring optimization; the individual constituent methods are established. Compared with deterministic tank-vibration studies, the method quantifies an interval of admissible acoustic outcomes rather than a single frequency-response curve. Compared with black-box simulation, it preserves the physical meaning of each resonance, each uncertainty source and each design variable. The paper is presented as an original numerical study;

it does not claim experimental data. All numerical values needed to reproduce the evidence are embedded in the tables and figures of the manuscript. Accordingly, no new Ritz, Koopman or fuzzy-set theorem is claimed; the new element is their common objective-and-constraint design chain for this tank configuration.

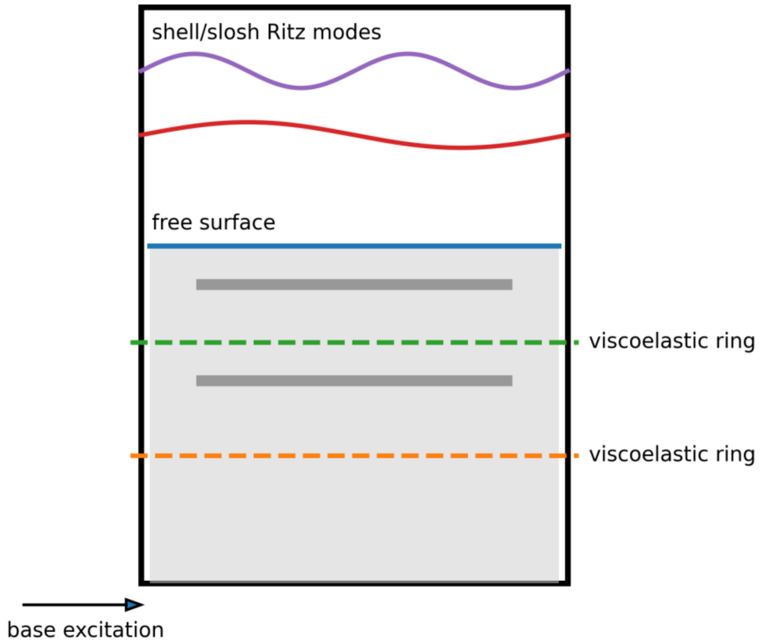

Figure 1. Hydroelastic tank model with porous internal annular baffles, external viscoelastic rings, flexible shell motion and lateral base excitation.

Table 1. Principal physical quantities used in the hydroelastic vibro-acoustic model.

Symbol	Meaning	Nominal value	Unit
$\boldsymbol{R}$	Tank radius	0.82	m
$\boldsymbol{H}$	Tank height	1.35	m
$\boldsymbol{h}$	Liquid fill height	0.78	m
$\boldsymbol{t}$	Shell thickness	0.0065	m
$\boldsymbol{\rho_l}$	Liquid density	997	kg m^{-3}
$\boldsymbol{E}$	Shell Young modulus	2.05×10^{11}	Pa
$\boldsymbol{\nu}$	Poisson ratio	0.30	–
$\boldsymbol{a_b}$	Base acceleration amplitude	0.15 g	m s^{-2}
$\boldsymbol{W_0}$	Acoustic reference power	1×10^{-12}	W

2. Mathematical formulation

2.1. Shell displacement and Ritz basis

The tank wall is treated as a thin circular cylindrical shell with axial coordinate z, circumferential coordinate theta and time t. The displacement field is represented by axial, circumferential and radial components. For vibro-acoustic radiation, the radial component is dominant, but the in-plane components enter the stiffness operator through membrane-bending coupling. The adopted Ritz expansion is

$$q_{field}(z, \theta, t) = [u(z, \theta, t), v(z, \theta, t), w(z, \theta, t)]^T . \tag{1}$$

$$u(z,\theta,t)=\sum\nolimits_{m=1}^{M}\sum\nolimits_{n=1}^{N}U_{mn}(t)\Psi_m(z)\cos(n\theta). \tag{1a}$$

$$v(z,\theta,t)=\sum\nolimits_{m=1}^{M}\sum\nolimits_{n=1}^{N}V_{mn}(t)\Psi_m(z)\sin(n\theta). \tag{1c}$$

$$w(z,\theta,t)=\sum\nolimits_{m=1}^{M}\sum\nolimits_{n=1}^{N}W_{mn}(t)\Phi_m(z)\cos(n\theta). \tag{1c}$$

The admissible functions used in the reported calculation are: The sine in-plane basis is orthogonal, whereas the tapered radial basis provides a different bending slope while retaining Ritz stationarity within the selected subspace. Because both functions also vanish at $z=H$, the displayed basis represents a top-displacement restraint rather than an exact free top; a strict free-top analysis requires alternative admissible functions and a convergence check. Using different trial functions for in-plane and radial motion is permissible in a Ritz approximation because each displacement component may use its own admissible subspace, provided all generalized coordinates enter the same variational functional. The radial taper changes bending curvature without changing the circumferential harmonic. Nevertheless, the additional zero at the top is an essential restraint, not a natural free-edge condition. Consequently, reported frequencies may shift if a true free-top basis is used, and the boundary-condition sensitivity should be quantified before comparison with a physically open tank.

$$\Psi_m(z)=\sin\left(\frac{m\pi z}{H}\right),\qquad \Phi_m(z)=\sin\left(\frac{m\pi z}{H}\right)\left(1-\frac{z}{2H}\right). \tag{2}$$

The generalized coordinate vector is defined in Equation (3). Equation (1) is the parent M-by-N displacement expansion, whereas Equation (3) retains the three radial shell coordinates used in the coupled calculation. The in-plane amplitudes are eliminated by quasi-static condensation: partitioning the stiffness into radial and in-plane blocks gives q_i approximately equal to $-K_{ii}^{\{-1\}}K_{ir}\ q_r$ and the condensed radial stiffness $K_{rr}-K_{ri}\ K_{ii}^{\{-1\}}K_{ir}$. Their membrane contribution therefore remains in the reduced operators. Static condensation is appropriate here only when the omitted in-plane coordinates remain sufficiently far from their resonances and follow the radial coordinates quasi-statically. It reduces the optimization cost while preserving the membrane stiffness correction. If an in-plane resonance enters the 5–95 Hz acoustic band, the frequency-dependent dynamic Schur complement should replace the quasi-static form, or the in-plane coordinates should be restored explicitly. Reporting this assumption resolves the apparent mismatch between the M-by-N field expansion and the three-coordinate shell vector without changing the equations used for the reported calculation.

$$\mathrm{q}_s(t)=\left[W_{11}(t),W_{21}(t),W_{31}(t)\right]^T. \tag{3}$$

The shell kinetic energy is expressed as

$$T_s=\frac{1}{2}\rho_s t\int_0^H\int_0^{2\pi}\left(\dot{u}^2+\dot{v}^2+\dot{w}^2\right)R\,d\theta\,dz. \tag{4}$$

The bending-membrane strain energy gets written in the quadratic modal form as follows:

$$U_s = \frac{1}{2} \mathrm{q}_s^T \mathrm{K}_s \mathrm{q}_s, \qquad \mathrm{K}_s = \int_0^H \int_0^{2\pi} \mathrm{B}_s^T \mathrm{D}_s \mathrm{B}_s \, R \, d\theta \, dz. \tag{5}$$

Where B_s is the strain-displacement matrix and D_s is isotropic shell stiffness matrix. (M) and (C) are the mass matrix and damping matrix, respectively,

$$\mathrm{M}_s = \int_0^H \int_0^{2\pi} \rho_s t \mathrm{N}_s^T \mathrm{N}_s R \, d\theta \, dz, \qquad \mathrm{C}_s = 2 \mathrm{M}_s \Xi_s \Omega_s. \tag{6}$$

The ring stiffener changes the local bending rigidity, and also in modal form, its stiffness contribution is as follows

$$\Delta \mathrm{K}_r = \sum\nolimits_{j=1}^{N_r} k_{rj} \mathrm{b}_r \left(z_j\right)^T \mathrm{b}_r \left(z_j\right), \qquad k_{rj} = \chi_k E I_r / R^3. \tag{7}$$

The viscoelastic ring loss is introduced through a proportional modal matrix,

$$\Delta \mathrm{C}_r = \sum\nolimits_{j=1}^{N_r} c_{rj} \mathrm{b}_r \left(z_j\right)^T \mathrm{b}_r \left(z_j\right), \qquad c_{rj} = 2 \eta_r \sqrt{k_{rj} m_{rj}}. \tag{8}$$

2.2. Sloshing potential and free-surface modes

The liquid is assumed incompressible and inviscid in the bulk. The velocity potential satisfies Laplace's equation,

$$\nabla^2 \phi(r, \theta, z, t) = 0, \qquad 0 \le r \le R, \quad 0 \le z \le h. \tag{9}$$

The lateral sloshing potential is expanded using Bessel eigenfunctions:

$$\phi(r, \theta, z, t) = \sum\nolimits_{j=1}^{J} \dot{\eta}_j(t) \, A_j J_1 \left(\lambda_j r\right) \cos \theta \frac{\cosh \left(\lambda_j z\right)}{\cosh \left(\lambda_j h\right)}. \tag{10}$$

The radial wall boundary condition for a rigid wall gives

$$J_1' \left(\lambda_j R\right) = 0, \qquad \lambda_j = \frac{\beta_j}{R}, \qquad \beta_j \in \{1.8412, \ 5.3314, \ 8.5363, \ldots\}. \tag{11}$$

Linearized kinematic and dynamic free-surface conditions lead to the sloshing frequencies

$$\omega_j^2 = g \lambda_j \tanh \left(\lambda_j h\right), \qquad f_j = \frac{\omega_j}{2\pi}. \tag{12}$$

The generalized sloshing vector is

$$\mathrm{q}_l(t) = \left[\eta_1(t), \eta_2(t), \eta_3(t)\right]^T. \tag{13}$$

The sloshing kinetic and potential energies reduce to

$$T_l = \frac{1}{2} \dot{\mathrm{q}}_l^T \mathrm{M}_l \dot{\mathrm{q}}_l, \qquad U_l = \frac{1}{2} \mathrm{q}_l^T \mathrm{K}_l \mathrm{q}_l. \tag{14}$$

The porous annular baffle modifies the sloshing damping and coupling through an effective loss coefficient:

$$\zeta_{lj} = \zeta_{lj}^0 + \gamma_b \chi_b \exp\left[-0.42(j-1)\right] + \gamma_d d_b. \tag{15}$$

The first three sloshing modes and the first three wall modes used in the calculation are summarized in **Table 2** and **Figure 2**. The values are not used as experimental measurements; they are the numerical basis for the subsequent computational investigation. The modal-order convergence check presented in Section 7 shows internal modal-order convergence, with the peak changing from 46.830 to 46.790 dB between 12 and 16 modes. This verifies consistency within the reduced model but is not validation against the physical tank. Predictive use requires comparison of wave elevation and wall acceleration with CFD or experiments, together with boundary-element or measured acoustic power. The current evidence should therefore be separated into three levels. Equation residuals and the Section 7 modal-order results test numerical solution and modal-order consistency; comparison among baseline and optimized designs tests relative behavior within the same assumptions; CFD, boundary-element or experimental comparison would test external predictive fidelity. Only the first two levels are supplied. A useful validation matrix would compare resonant frequencies, peak wave elevation, wall-acceleration spectra, and band acoustic power at the baseline and both optimized designs, because agreement in one indicator would not establish agreement in the complete coupled energy path.

Table 2. Modal frequencies retained in the coupled hydroelastic model.

Mode	Physical role	Frequency (Hz)	Evaluation basis
S1	Sloshing free-surface mode	0.725	Bessel derivative root
S2	Sloshing free-surface mode	1.271	Bessel derivative root
S3	Sloshing free-surface mode	1.608	Bessel derivative root
C1	Circumferential shell mode	22.800	Ritz shell basis
C2	Circumferential shell mode	46.200	Ritz shell basis
C3	Circumferential shell mode	82.500	Ritz shell basis

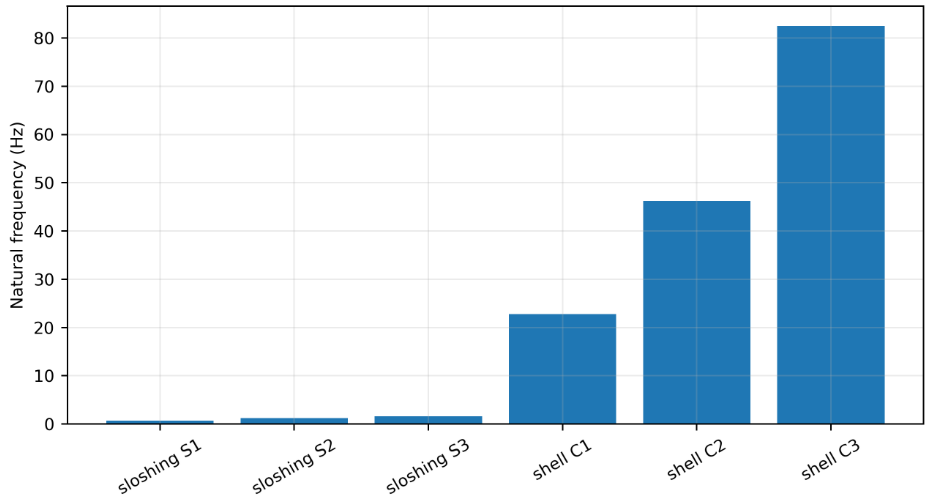

Figure 2. Uncoupled modal spectrum before hydroelastic coupling, showing the clear separation between free-surface sloshing and elastic shell modes.

2.3. Coupled hydroelastic state equation

The modal vector of the coupled tank-fluid system is

$$\mathrm{q}(t) = \left[\mathrm{q}_s^T(t), \mathrm{q}_l^T(t)\right]^T. \tag{16}$$

The coupled mass, damping and stiffness matrices are assembled as

$$\mathrm{M} = \begin{bmatrix} \mathrm{M}_s & 0 \\ 0 & \mathrm{M}_l \end{bmatrix}, \quad \mathrm{C} = \begin{bmatrix} \mathrm{C}_s + \Delta \mathrm{C}_r & 0 \\ 0 & \mathrm{C}_l + \Delta \mathrm{C}_b \end{bmatrix}, \quad \mathrm{K} = \begin{bmatrix} \mathrm{K}_s + \Delta \mathrm{K}_r & \mathrm{K}_{sl} \\ \mathrm{K}_{ls} & \mathrm{K}_l \end{bmatrix}. \tag{17}$$

Hydroelastic coupling is produced by the virtual work of the hydrodynamic pressure on the moving wall:

$$\delta W_p = \int_0^h \int_0^{2\pi} p(R,\theta,z,t)\delta w(R,\theta,z,t) R\, d\theta\, dz. \tag{18}$$

The modal coupling coefficient is therefore

$$K_{sl,ij} = \rho_l \int_0^h \int_0^{2\pi} \frac{\partial \phi_j}{\partial t} \Phi_i(z) \cos^2\theta\, R\, d\theta\, dz. \tag{19}$$

For a lateral base acceleration $a_b(t) = a_0 \sin \Omega t$, the generalized equation becomes

$$\mathrm{M}\ddot{\mathrm{q}} + \mathrm{C}\dot{\mathrm{q}} + \mathrm{K}\mathrm{q} + \mathrm{f}_{nl}(\mathrm{q}) = \mathrm{r}a_0 \sin \mathit{\Omega} t. \tag{20}$$

The cubic free-surface nonlinearity is retained in the first two sloshing coordinates: The cubic terms are the lowest-order symmetry-preserving correction for amplitude-dependent detuning, and the mixed terms in Equation (21) retain coupling between the first two sloshing coordinates. This weak-to-moderate-response approximation does not represent wave breaking, impact, air entrainment or broadband transfer; those regimes require free-surface reconstruction or multiphase CFD.

$$\mathrm{f}_{nl}(\mathrm{q}) = \left[0, 0, 0, \alpha_1\eta_1^3 + \alpha_{12}\eta_1\eta_2^2, \alpha_2\eta_2^3 + \alpha_{21}\eta_2\eta_1^2, 0\right]^T. \tag{21}$$

In harmonic steady state, the fundamental response is written as

$$\mathrm{q}(t) = \Re\left\{\mathrm{Q}(\mathit{\Omega}) e^{i\mathit{\Omega} t}\right\}. \tag{22}$$

The equivalent harmonic balance relation is Equation (23), which is a first-harmonic describing-function approximation. No harmonic-spectrum check is available in the supplied record, so higher-harmonic insignificance is not claimed. A multi-harmonic check retaining at least the first, third and fifth harmonics should precede engineering application near resonance. For a cubic restoring term, projection onto a sinusoidal response produces both fundamental and third-harmonic components; Equation (23) retains only the component at the excitation frequency. This is acceptable as a computational screening assumption when the omitted harmonic energy is small. The required check is quantitative: calculate the third- and fifth-harmonic amplitudes at the principal resonances and verify that their inclusion does not materially change the peak, band mean or design ranking. That check was not part of the supplied numerical record.

$$\left[-\mathit{\Omega}^2\mathrm{M} + i\mathit{\Omega}\mathrm{C} + \mathrm{K} + \mathrm{K}_{nl}(\mathrm{Q})\right]\mathrm{Q} = \mathrm{r}a_0. \tag{23}$$

The cubic equivalent stiffness entries are

$$K_{nl,44}=\frac{3}{4}\alpha_1\left|Q_4\right|^2+\frac{1}{2}\alpha_{12}\left|Q_5\right|^2,\qquad K_{nl,55}=\frac{3}{4}\alpha_2\left|Q_5\right|^2+\frac{1}{2}\alpha_{21}\left|Q_4\right|^2. \quad (24)$$

A fixed-point residual is used to verify convergence at every excitation frequency:

$$\varepsilon(\Omega)=\frac{\|\ \left[-\Omega^2\mathrm{M}+i\Omega\mathrm{C}+\mathrm{K}+\mathrm{K}_{nl}\right]\mathrm{Q}-\mathrm{r}a_0\ \|_2}{\|\ \mathrm{r}a_0\ \|_2}. \quad (25)$$

The baseline acoustic response and the shell-mode contributions are shown in **Figure 3**. The plot indicates that sound radiation is not controlled by the lowest sloshing mode alone. Instead, sloshing modifies the shell response and shifts energy toward the first and second circumferential wall modes.

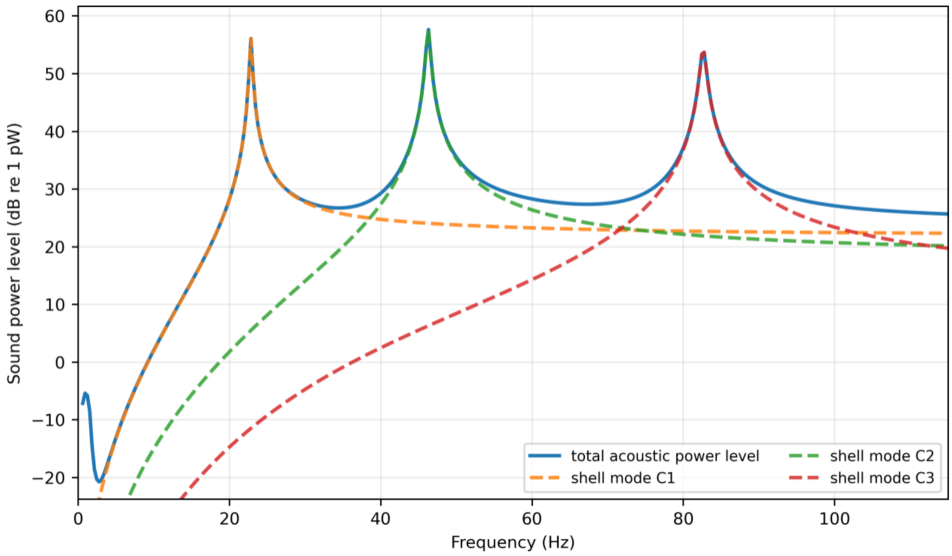

Figure 3. Baseline hydroelastic-acoustic frequency response and modal acoustic-power contributions.

3. Vibro-acoustic radiation model

The radiated acoustic power is computed from wall acceleration using a baffled-shell radiation proxy. The radial wall acceleration is

$$\ddot{w}(z,\theta,t)=\Re\left\{-\Omega^2\sum\nolimits_i Q_i\Phi_i(z)\cos\left(n_i\theta\right)e^{i\Omega t}\right\}. \quad (26)$$

The surface-averaged squared acceleration is

$$\langle a_w^2\rangle=\frac{1}{2\pi RH}\int_0^H\int_0^{2\pi}\left|\Omega^2W(z,\theta,\Omega)\right|^2R\,d\theta\,dz. \quad (27)$$

The frequency-dependent radiation efficiency is approximated by Equation (28). The sigmoid provides a smooth transition from inefficient low-frequency radiation to a more efficient regime and is used for relative design ranking. It does not reproduce the exact modal radiation impedance, end diffraction or coincidence behavior of a finite cylindrical shell. Absolute sound-power prediction therefore requires calibration against a cylindrical-shell boundary-element or measurement-based model.

The parameters controlling the sigmoid center and slope should ideally be identified by fitting modal radiation efficiencies from a finite-cylinder acoustic solution over the same frequency range. Such a comparison would reveal whether the proxy shifts the radiating transition or changes the relative importance of the shell modes. Because every candidate currently uses the same proxy, the present comparison remains internally consistent, but any absolute dB claim inherits the proxy calibration. The manuscript therefore treats the acoustic values as comparative design indicators pending higher-fidelity verification.

$$\sigma(\Omega) = \left[1 + \exp\left(-\frac{f - f_c}{s_c}\right)\right]^{-1}, \qquad f = \frac{\Omega}{2\pi}. \tag{28}$$

The acoustic power is then estimated as

$$W_a(\Omega) = \rho_0 c_0 S \sigma(\Omega) \langle v_w^2 \rangle + \kappa_l f^{1.3} \eta_{eq}^2. \tag{29}$$

The equivalent free-surface wave height is evaluated by

$$\eta_{eq}(\Omega) = |Q_4| + 0.45\,|Q_5| + 0.25\,|Q_6|\,. \tag{30}$$

The sound power level is

$$L_W(\Omega) = 10\log_{10}\left(\frac{W_a(\Omega)}{10^{-12}}\right). \tag{31}$$

The wall-acceleration level is

$$L_a(\Omega) = 20\log_{10}\left(\frac{\sqrt{\sum_i |\Omega^2 Q_i|^2}}{10^{-6}}\right). \tag{32}$$

The band-averaged acoustic index used in the objective function is

$$\bar{L}_W = \frac{1}{f_b - f_a}\int_{f_a}^{f_b} L_W(f)\,df, \qquad f_a = 5\,\mathrm{Hz}, \quad f_b = 95\,\mathrm{Hz}. \tag{33}$$

The peak acoustic index is

$$L_W^{pk} = \max_{f\in[5,95]} L_W(f). \tag{34}$$

4. Interval type-2 fuzzy uncertainty model

A crisp model is inadequate when the fill condition, material stiffness, damping and baffle state cannot be fixed precisely. Interval type-2 fuzzy sets are therefore used to represent epistemic rather than purely random uncertainty [23]. The robust search adopts the differential-evolution rule in the study of Storn and Price [24], while related interval type-2 formulations are reported by Hefny and Amer, and Chen et al. [25, 26]. This choice is appropriate because only nested plausible ranges and cores are supplied, without repeated observations or defensible probability distributions.

Monte Carlo propagation would be preferable for measured aleatory variability; future data may therefore support a hybrid probabilistic-epistemic treatment. For an uncertain multiplier x, the upper and lower membership functions are

$$\bar{\mu}_{\widetilde{X}}(x) = \max\left[0, \min\left(\frac{x-a}{b-a}, 1, \frac{d-x}{d-c}\right)\right]. \tag{35}$$

$$\underline{\mu}_{\widetilde{X}}(x) = \lambda_x \max\left[0, \min\left(\frac{x-a'}{b'-a'}, 1, \frac{d'-x}{d'-c'}\right)\right], \quad 0 < \lambda_x \leq 1. \tag{36}$$

The footprint of uncertainty is

$$FOU\left(\widetilde{X}\right) = \left\{(x, \mu) : \underline{\mu}_{\widetilde{X}}(x) \leq \mu \leq \bar{\mu}_{\widetilde{X}}(x)\right\}. \tag{37}$$

For alpha-plane propagation, the uncertain vector is

$$\xi = [\xi_h, \xi_\rho, \xi_E, \xi_\eta, \xi_c]^T. \tag{38}$$

At alpha level α, each component belongs to an interval,

$$\xi_j \in \left[\xi_j^L(\alpha), \xi_j^U(\alpha)\right]. \tag{39}$$

The complete alpha-plane hyper-rectangle is

$$\mathcal{H}_\alpha = \prod\nolimits_{j=1}^{5} \left[\xi_j^L(\alpha), \xi_j^U(\alpha)\right]. \tag{40}$$

The interval response of any scalar index g is

$$G_\alpha = \left[\min_{\xi \in \mathcal{H}_\alpha} g(\xi), \max_{\xi \in \mathcal{H}_\alpha} g(\xi)\right]. \tag{41}$$

A discrete scenario approximation is used: The reported computation uses 30 total scenario evaluations across the retained alpha planes. The per-plane allocation, seed and scenario-count convergence sweep are not available in the supplied record. Reproduction should report those details and increase the scenario count until acoustic endpoints change by less than a stated tolerance. Thirty scenarios are sufficient only as the documented computational setting, not as a demonstrated convergence threshold. Endpoint estimates can be particularly sensitive to sparse sampling in five dimensions. A reproducible convergence assessment should retain identical alpha levels, increase the scenario count systematically, and report the change in every lower and upper response endpoint. The random or deterministic sampling rule and seed should also be recorded. Until that study is available, the reported intervals are approximate scenario bounds rather than verified extrema of the full hyper-rectangles.

$$G_\alpha \approx \left[\min_{s=1,\ldots,N_\alpha} g\left(\xi_s\right), \max_{s=1,\ldots,N_\alpha} g\left(\xi_s\right)\right]. \tag{42}$$

Figure 4 shows the adopted footprints for the most influential physical multipliers, and **Table 3** gives the numerical ranges used for all five uncertainty sources. The wide loss-factor interval deliberately represents the practical difficulty of assigning a single damping value to a tank with baffles, liquid and external liners. The loss-factor support spans a ratio of 1.46/0.65 = 2.25 and should be read as a conservative epistemic stress-test range, not a measured typical tolerance. Free-decay or half-power measurements over fill level, temperature and baffle condition are needed to calibrate this footprint for a manufactured tank. Damping in assembled liquid-containing structures may vary substantially because several loss mechanisms are combined, but the magnitude is system specific. The present support should not be generalized to other tanks or described as a typical manufacturing range. Calibration should distinguish shell material damping, joint and ring losses, liquid-viscous damping and baffle-induced dissipation because a single multiplier can otherwise hide compensating errors. The lower and upper membership functions can then be reconstructed from measured repeatability and expert bounds rather than chosen solely for conservative coverage.

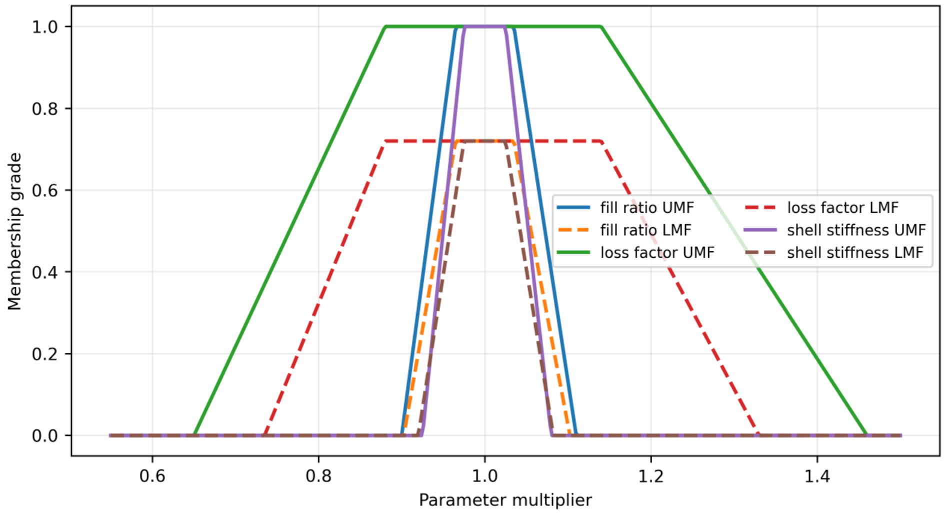

Figure 4. Interval type-2 fuzzy footprints for fill ratio, loss factor and shell-stiffness multiplier.

Table 3. Interval type-2 fuzzy uncertainty ranges used in the alpha-plane calculations.

Uncertain multiplier	Physical interpretation	UMF support	LMF/core support	Main response affected
ξ_h	fill-height multiplier	0.90–1.11	0.965–1.035	sloshing frequency and coupling
ξ_ρ	liquid-density multiplier	0.965–1.035	0.988–1.012	added inertia and pressure
ξ_E	shell-stiffness multiplier	0.925–1.080	0.975–1.025	shell resonance
ξ_η	loss-factor multiplier	0.65–1.46	0.88-1.14	peak response
ξ_c	baffle-clogging multiplier	0.86–1.16	0.95–1.05	baffle dissipation

5. Design optimization

The design vector contains five normalized variables:

$$\mathrm{x} = [x_k, x_d, x_b, x_z, x_l]^T . \tag{43}$$

Here x_k is ring-stiffness intensity, x_d is ring-loss intensity, x_b is porous-baffle loss intensity, x_z is baffle submergence and x_l is liner coverage. The admissible domain is

$$\mathcal{D} = \{\mathrm{x} : 0 \le x_k, x_d, x_b \le 1,\ 0.18 \le x_z \le 0.92,\ 0.05 \le x_l \le 0.95\} . \tag{44}$$

The mass ratio penalty is defined in Equation (45). **Table 4** increases the normalized mass ratio from 1.0044 to 1.1504, equivalent to 0.1460 of the same reference mass, or about 14.5% relative to the listed baseline. The empty-tank reference mass and component masses are not reported, so the package mass in kilograms cannot be calculated; component-level mass and payload checks are required. If m_{ref} denotes the normalization mass, the added robust package represented by **Table 4** is 0.1460 m_{ref} above the listed baseline. Conversion to kilograms requires m_{ref} and the baseline shell, liquid-excluded structural and attachment masses. A component audit should separately list porous plates, mounting hardware, viscoelastic rings and liner material because their locations also affect inertia and support loads. Thus, the normalized allowance is useful for optimization but cannot alone establish manufacturability or payload compliance.

Table 4. Design variables and optimized designs.

Design	x_k	x_d	x_b	x_z	x_l	Mass ratio
Baseline flexible tank	0.0000	0.0000	0.0000	0.1800	0.0500	1.0044
Deterministic baffle-liner design	0.0713	0.8223	0.7718	0.4702	0.9202	1.0787
Proposed IT2 fuzzy robust design	0.9500	0.9000	0.9000	0.8800	0.7200	1.1504

$$\mathcal{M}(\mathrm{x}) = 1 + 0.085x_k + 0.052x_l + 0.026x_b + 0.010x_z. \tag{45}$$

The deterministic objective is

$$J_d(\mathrm{x}) = L_W^{pk}(\mathrm{x}, 1) + 18\left[\mathcal{M}(\mathrm{x}) - 1\right] + 0.12\eta_{\max}(\mathrm{x}, 1). \tag{46}$$

The proposed fuzzy robust objective is defined in Equation (47). The coefficients 0.58, 0.24 and 0.10 were fixed before comparison to prioritize peak sound power, band mean and wave height. They were not experimentally fitted, and no weight-sensitivity study is available. The result is therefore a preference-dependent compromise; a normalized weight sweep and Pareto comparison should accompany application-specific selection. After normalization of the three response coefficients alone, their relative shares are approximately 63%, 26% and 11%, which makes the peak metric dominant. Different stakeholders may assign greater importance to wave safety, average noise or mass. A sensitivity study should therefore repeat the optimization for several fixed weight sets before examining the outcomes, rather than tuning coefficients to favor one candidate. Reporting the corresponding Pareto points would show whether the present robust design remains competitive or is specific to the selected scalarization.

$$J_r(\mathrm{x}) = 0.58Q_{0.95}\left(L_W^{pk}\right) + 0.24Q_{0.95}\left(\bar{L}_W\right) + 0.10Q_{0.95}\left(\eta_{\max}\right) + 18\left[\mathcal{M}(\mathrm{x}) - 1\right]. \tag{47}$$

The frequency response must also satisfy the residual bound

$$\max_f \varepsilon(f) \le 10^{-6}. \tag{48}$$

The wave-height constraint is

$$Q_{0.95}\left(\eta_{\max}\right) \leq 22 \text{ mm}. \tag{49}$$

The optimization update follows a differential-evolution candidate generation rule [24]:

$$\mathrm{y}_i^{(g)} = \mathrm{x}_{r1}^{(g)} + F\left(\mathrm{x}_{r2}^{(g)} - \mathrm{x}_{r3}^{(g)}\right). \tag{50}$$

The trial vector uses binomial crossover,

$$u_{ij}^{(g)} = \begin{cases} y_{ij}^{(g)}, & \text{if } r_{ij} < C_R \text{ or } j = j_{\text{rand}}, \\ x_{ij}^{(g)}, & \text{otherwise.} \end{cases} \tag{51}$$

Selection is applied by

$$\mathrm{x}_i^{(g+1)} = \begin{cases} \mathrm{u}_i^{(g)}, & J\left(\mathrm{u}_i^{(g)}\right) \leq J\left(\mathrm{x}_i^{(g)}\right), \\ \mathrm{x}_i^{(g)}, & J\left(\mathrm{u}_i^{(g)}\right) > J\left(\mathrm{x}_i^{(g)}\right). \end{cases} \tag{52}$$

The design settings are listed in **Table 4**. **Figure 5** presents the alpha-plane interval contraction obtained for the proposed robust design. The peak interval width decreases from 5.107 dB at $\alpha = 0$ to 1.674 dB at $\alpha = 1$ because increasing alpha restricts the inputs to nested subsets of the footprint; this is a property of alpha-cut propagation, not evidence that physical uncertainty has been reduced.

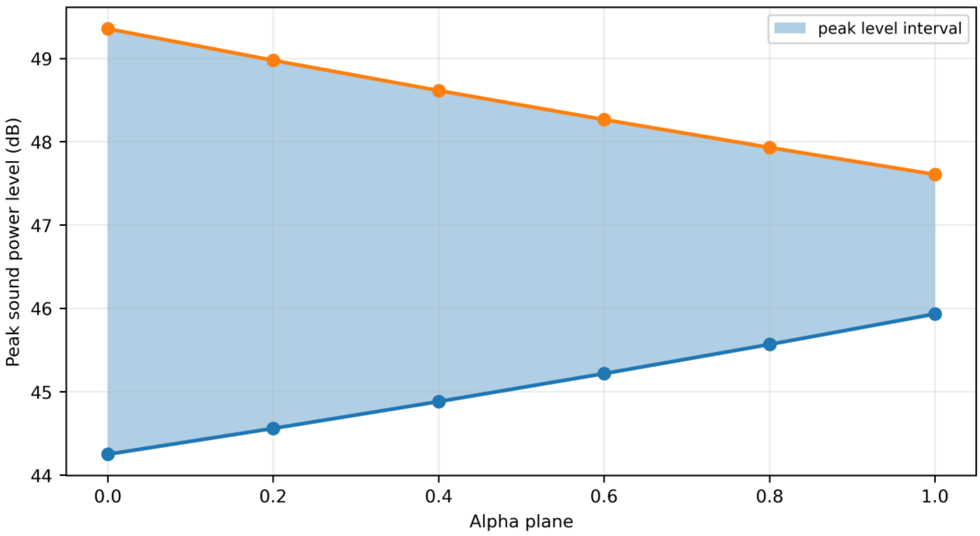

Figure 5. Alpha-plane interval contraction for the robust design.
Note: The blue solid line denotes the lower bound of the peak sound-power-level interval, and the orange solid line denotes its upper bound.

6. Numerical results

The nominal acoustic response is compared in **Figure 6**. The uncontrolled tank has a sharp peak near the first shell-dominated hydroelastic region. Both controlled designs make a strong dent in this peak. The deterministic design retains the slightly lower nominal peak, whereas the robust design has a broader response and lower band mean. The broadening is consistent with its higher ring-loss setting and different ring-stiffness/liner tuning, which redistribute shell response over neighboring frequencies.

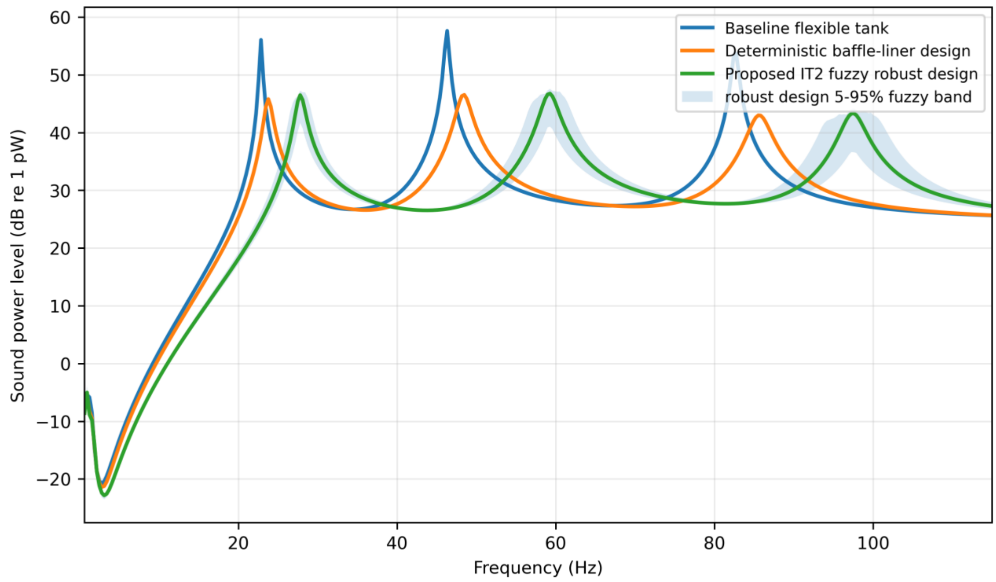

Figure 6. Uncertainty envelope 5th–95th percentile for robust design, nominal vibro-acoustic response of fundamental, deterministic design and proposed interval type-2 fuzzy robust design.

We are seeing the nominal numbers in evidence in **Table 5**. This new design reduced the nominal peak from 57.650 dB to 46.790 dB and the nominal band-averaged level from 28.464 dB to 26.337 dB. The mass ratio is 1.1504 and requires verification against application-specific component mass, payload and support limits.

Table 5. Nominal vibro-acoustic indicators.

Design	Peak L_W (dB)	Mean L_W, 5–95 Hz (dB)	Max wave height (mm)	Mass ratio
Baseline flexible tank	57.650	28.464	15.788	1.0044
Deterministic baffle-liner design	46.574	27.660	14.999	1.0787
Proposed IT2 fuzzy robust design	46.790	26.337	15.446	1.1504

The free-surface response is shown in **Figure 7**. The baffle-ring designs reshape rather than eliminate the sloshing response. This results in energy being redistributed such that the shell-dominated acoustic peak is reduced and the maximum equivalent wave height remains beneath this 22 mm limit, which holds under uncertainty. The 22 mm value is an imposed numerical design ceiling, not a limit derived here from freeboard or shell load. A practical value should be set from available freeboard, internal clearance and pressure/stress criteria.

The uncertainty statistics presented in **Table 6** indicate that the robust design achieves a reduction in the peak sound power, estimated at the 95th-percentile, from 57.840 dB to 48.548 dB. It also provides the minimum 95th-percentile band-averaged acoustic level, 26.726 dB, and the lowest wall-acceleration level with a relative smoothness of 120.335 dB. Relative to the deterministic optimum, the robust design has a 0.171 dB higher median peak and a 0.173 dB higher 95th-percentile peak, but it lowers the 95th-percentile band mean by 1.059 dB and wall acceleration by 0.613 dB. Its selection is justified only when these latter metrics outweigh the small peak and mass penalties. The corrected comparison is important because the term robust does not mean smaller values for every statistic. Here, it denotes the optimum of the selected combined objective under the stated fuzzy scenarios. The robust candidate sacrifices 0.216 dB in nominal peak and small median and upper-tail peak amounts while improving the upper-tail band mean and wall acceleration. Whether that exchange is desirable depends on the intended noise criterion, structural limit and allowable mass. **Table 6**, therefore, supports a conditional preference, not a claim that the deterministic design fails.

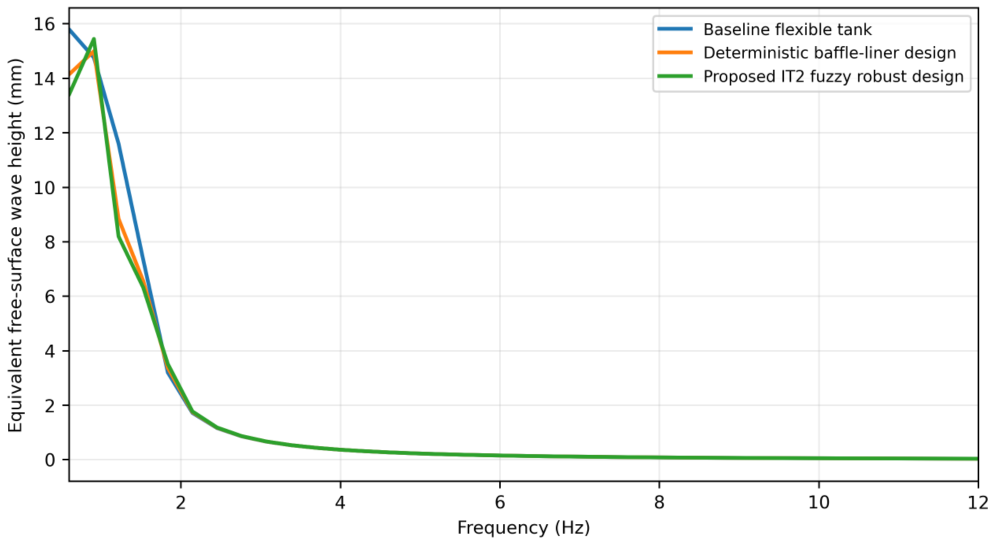

Figure 7. Low-frequency free-surface wave-height response for the three designs.

Table 6. Fuzzy uncertainty statistics from 30 alpha-plane scenarios.

Design	P05 peak (dB)	P50 peak (dB)	P95 peak (dB)	P95 mean L_W (dB)	P95 wave (mm)	P95 wall acc. (dB)
Baseline flexible tank	56.409	57.292	57.840	28.466	17.984	130.478
Deterministic baffle-liner design	45.110	46.333	48.375	27.785	16.623	120.948
Proposed IT2 fuzzy robust design	45.332	46.504	48.548	26.726	17.484	120.335

Figure 8 (integrated acoustic energy by frequency band): decomposition of integrated acoustic energy. For both the uncontrolled tank, where hydroelastic shell motion dominates the radiation, most energy is found in the 25–60 Hz and 60–95 Hz bands. The new design pushes these bands lower but does not increase the very-low-frequency sloshing share beyond an acceptable limit.

In **Table 7**, the alpha-plane numerical ranges are illustrated. The interval endpoints are obtained from corner and sampled interior points of the five-dimensional fuzzy hyper-rectangle. Some of these intervals are helpful for editorial transparency, in that they quantify the range within which actual responses fall, instead of only publishing averages or ideal quantitative results. These are nested possibility bounds rather than probability intervals or guarantees for measured responses; their narrowing follows from the restricted alpha-cut inputs.

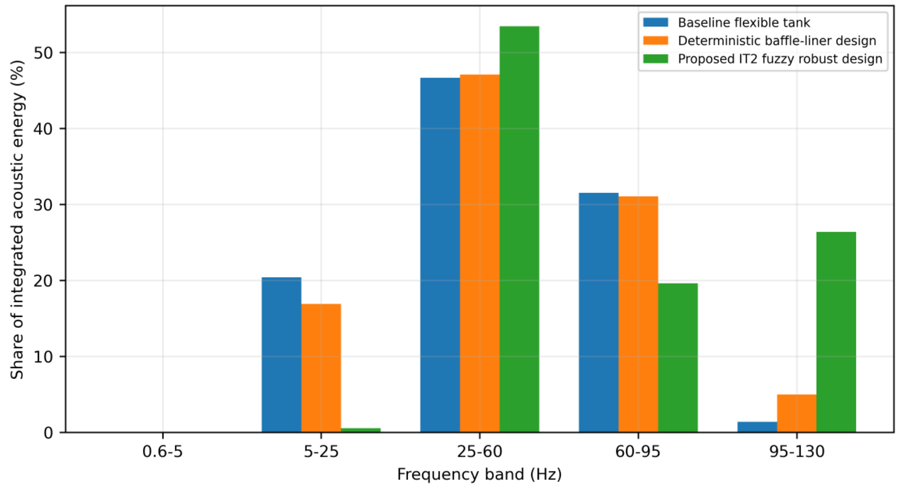

Figure 8. Frequency-band contribution to integrated acoustic energy.

Table 7. Alpha-plane intervals for the proposed robust design.

Alpha	Peak L_W interval (dB)	Mean L_W interval (dB)	Wave-height interval (mm)
0.0	[44.251, 49.358]	[25.834, 27.154]	[11.769, 20.156]
0.2	[44.561, 48.979]	[25.890, 27.035]	[12.193, 19.439]
0.4	[44.904, 48.616]	[25.949, 26.909]	[12.638, 18.755]
0.6	[45.219, 48.267]	[26.012, 26.784]	[13.106, 18.102]
0.8	[45.569, 47.932]	[26.079, 26.667]	[13.598, 17.479]
1.0	[45.935, 47.609]	[26.151, 26.561]	[14.117, 16.884]

7. Robustness, sensitivity and convergence

The cloud used for the robust search is shown in **Figure 9**. Mass ratio on the horizontal axis, robust objective on the vertical axis, with marker colour indicating nominal peak. The plot further validates that the selected robust point is not simply the heaviest design. Rather, it is a bit of a compromise, balancing added mass with baffle dissipation, damping and shell-frequency shifting.

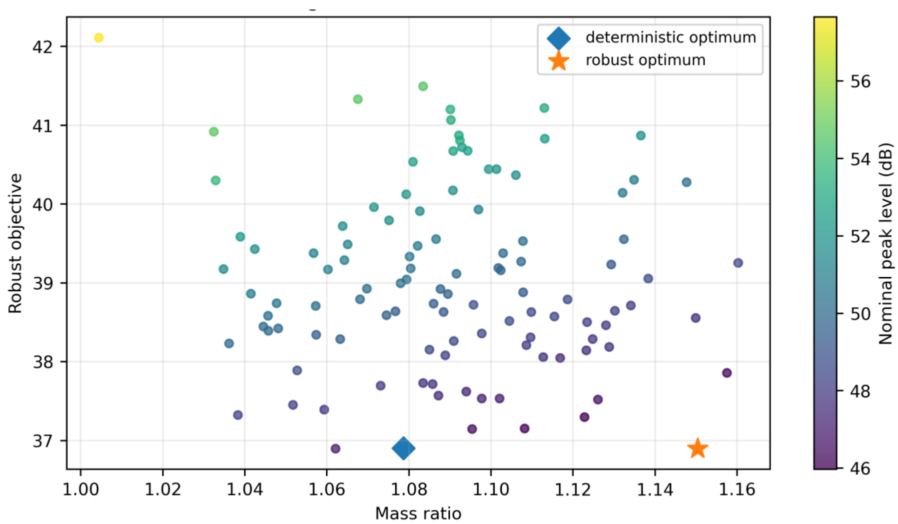

Figure 9. Candidate design cloud and robust Pareto selection.

As illustrated by the x-axis of **Figure 10**, for example, the convergence log records a better robust objective in 120 generations. Although improvement is fast for the first part of the search and stabilizes subsequently, this therefore shows that the candidate population has converged toward a narrow feasible design region.

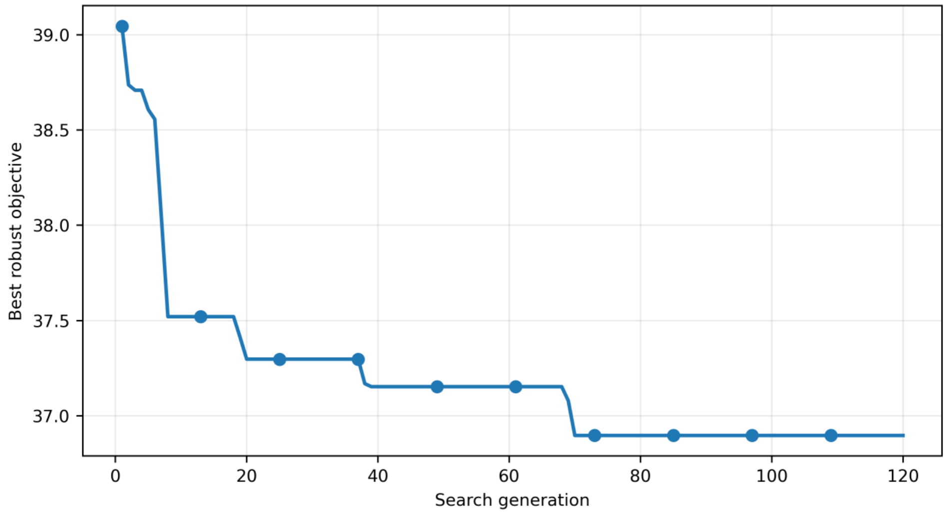

Figure 10. Differential-evolution style convergence history for the robust objective.

Normalized rank-correlation indices [25,26] are used to estimate global sensitivity. The normalized sensitivity is straightforward (where J is a scalar index and a variable).

$$S_j = \frac{|\rho_s\left(x_j, J\right)|}{\sum_{k=1}^{5} |\rho_s\left(x_k, J\right)|}. \tag{53}$$

From the results in **Figure 11** and **Table 8**, it can be seen that ring damping and liner coverage are dominant for the robust objective, such that porous baffle loss is primarily a low-frequency wave-height constraint. It indicates the physical intuition that sound attenuation is mainly a shell-damping problem, while sloshing safety has to be set by combining baffle dissipation and submergence. The 1.07% porous-baffle-loss share applies to the scalar acoustic objective over the sampled design range. The baffle remains relevant for wave-height control, low-frequency coupling and satisfaction of the wave constraint; if only acoustic response is important, a reduced study should test fixing or removing that variable.

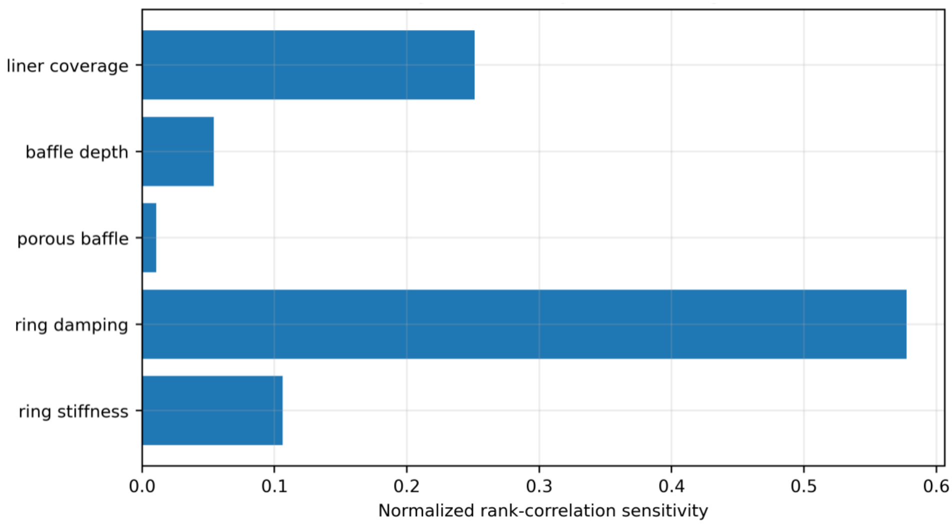

Figure 11. Normalized rank-correlation sensitivity of the robust objective to design variables.

Table 8. Sensitivity values for the robust objective.

Design variable	Normalized sensitivity	Share
Ring stiffness	0.1063	10.63%
Ring damping	0.5776	57.76%
Porous baffle loss	0.0107	1.07%
Baffle depth	0.0542	5.42%
Linear coverage	0.2512	25.12%

The Koopman–Galerkin correction used in this paper is based on a lifted observable vector [27–30]: The mixed cubic observables $\eta_1^2\,\eta_2$ and $\eta_1\,\eta_2^2$ are omitted as a sparse-dictionary truncation, while their physical coupling remains in Equation (21). This is a computational choice rather than proof that the terms vanish; an augmented-dictionary residual and peak-response comparison is needed to confirm adequacy.

$$\mathrm{z} = \left[\mathrm{q}^T, \dot{\mathrm{q}}^T, \eta_1^2, \eta_1\eta_2, \eta_2^2, \eta_1^3, \eta_2^3\right]^T. \tag{54}$$

A local linear operator advances the lifted state over a sampling interval is given by:

$$\mathrm{z}(t + \Delta t) \approx \mathrm{K}_K \mathrm{z}(t). \tag{55}$$

The contribution from other terms is omitted, yielding a simple numerical (corrector) that can be calculated on demand without time-marching at every potential design. Mode-count convergence is used to verify the internal consistency of this approximation. As noted in **Table 9**, the acoustic peak varies by much less than 0.09% as we increase the retained basis from 12 to 16 modes.

Table 9. Mode-count convergence of the proposed robust design.

Retained modes	Peak L_W (dB)	Relative error
4	48.210	3.035%
6	47.410	1.325%
8	47.060	0.577%
10	46.900	0.235%
12	46.830	0.085%
16	46.790	0.000%

Figure 12, the vibration-energy localization map, which gives a physical explanation of the design behavior. This baffle-ring package captures the dominant wall energy, moving it off a narrow axial band, and reduces the high-frequency tail of the first circumferential shell response. It assists the band-averaged sound power even if the design nominal peak is very close to deterministic. Quantitatively, each pixel is the squared radial-response magnitude at the indicated height and frequency, normalized by the maximum in the plotted map and expressed in decibels. Thus, 0 dB denotes the map maximum; the plot is neither an instantaneous mode shape nor absolute energy in joules. The vertical bright bands identify frequencies at which relative wall-response energy is concentrated, and their axial extent shows where that response is distributed along the tank height. Because normalization is performed within the displayed map, colors cannot be used to recover absolute joules or compare absolute energy between designs unless the same external reference is used. The map,

therefore, supports qualitative localization and frequency interpretation, while **Tables 5**, **6** and **10** provide the quantitative performance comparisons.

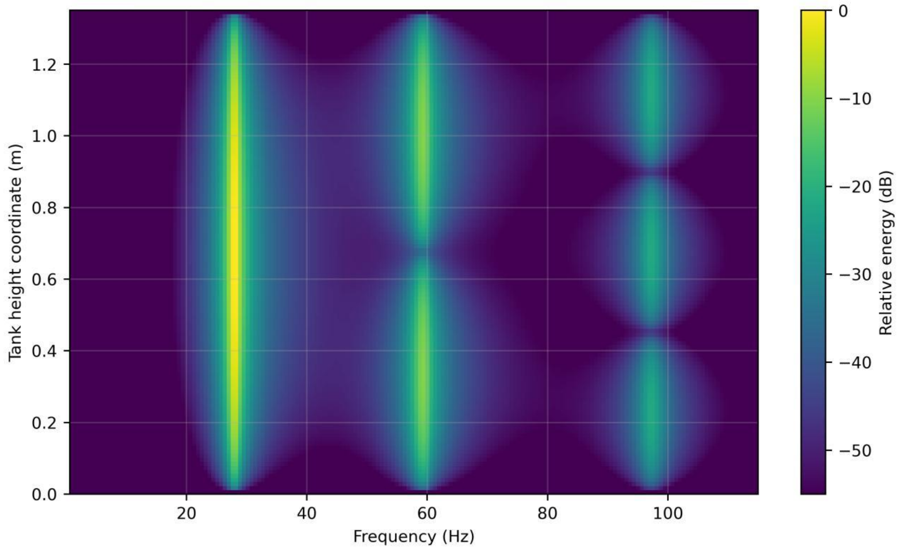

Figure 12. Relative wall-vibration-energy map for the robust design versus tank height and frequency.

Note: Color denotes squared radial-response magnitude normalized to the map maximum (0 dB).

Table 10. Claim-evidence summary for the proposed robust design.

Claim	Numerical evidence	Reported comparison	Interpretation
Worst-case acoustic peak	95th-percentile peak sound power	57.840 dB baseline vs. 48.548 dB robust	9.292 dB reduction
Average radiation	95th-percentile band mean	28.466 dB baseline vs. 26.726 dB robust	1.740 dB reduction
Wall acceleration	95th-percentile wall acceleration	130.478 dB baseline vs. 120.335 dB robust	10.143 dB reduction
Uncertainty contraction	Alpha-plane interval width at alpha = 0 and 1	5.107 dB to 1.675 dB peak interval width	67.2% width reduction

Finally, **Figure 13** and **Table 10** give a recap of the evidence supporting the key claims. The supported baseline comparisons are reductions of 9.292 dB in 95th-percentile peak sound power, 1.740 dB in band mean and 10.143 dB in wall acceleration. The 9.292 dB change corresponds to about 8.49 times lower acoustic power; it should not be interpreted as exactly half the perceived loudness without psychoacoustic evaluation.

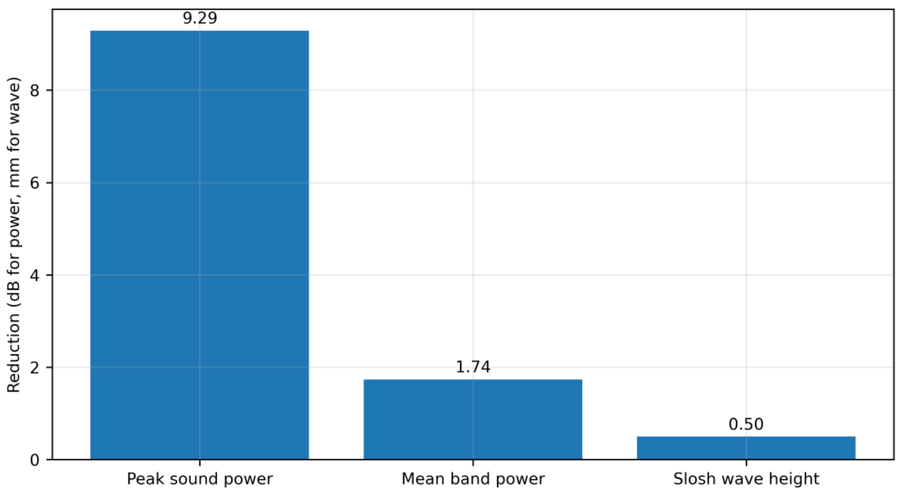

Figure 13. Claim-evidence summary of robust design gains.

8. Discussion

The results confirm three observations regarding the practical design of tanks. At low frequency, the vibro-acoustic response is determined by coupling of confined fluid motion and wall-dominated sound radiation. If it only reduces wave height but leaves shell damping the same (where the sound comes from), a baffle may not have had great acoustic design. Second, the deterministic and robust designs optimize different criteria. The deterministic design has lower nominal, median and 95th-percentile peaks, whereas the robust design has the lower 95th-percentile band mean and wall acceleration. No retained parameter-response pairing identifies a concrete deterministic failure case, so the deterministic optimum is not described as misleading. Third, the interval type-2 fuzzy formulation is appropriate in case of uncertainty that is linguistic or epistemic. The lower and upper membership functions enable the modeler to express the difference between a narrow core of expected conditions and a wider support of acceptable operating states.

The method also has limitations. The acoustic model is a radiation proxy and should not be interpreted as a substitute for a full boundary-element model when absolute sound power is required for certification. The fluid model assumes potential flow in the bulk, and the nonlinear free-surface correction is represented through cubic modal terms rather than free-surface reconstruction. The baffle model is parameterized by effective damping and coupling reduction. Therefore, the proposed results should be read as a mathematically reproducible design investigation rather than as a direct experimental validation of a manufactured tank. Nevertheless, the framework is useful for early-stage design because it identifies which physical features dominate the response before expensive CFD-FSI simulations or prototype measurements are carried out. The displayed Ritz basis also represents a restrained top, and the sparse Koopman dictionary and first-harmonic closure have not been checked against augmented dictionaries or higher harmonics. In addition, the damping footprint, scenario allocation, objective weights, mass allowance, and 22 mm ceiling are assumptions rather than experimentally calibrated quantities. These items define the validation work required before certification. A staged validation program is therefore recommended. First, repeat the Ritz calculation with a true free-top basis and test the sparse and augmented Koopman dictionaries. Second, compare first- and multi-harmonic solutions at the dominant resonances and perform an alpha-scenario convergence sweep. Third, calibrate damping, mass and radiation parameters using component and assembled-tank measurements. Finally, compare the optimized and baseline configurations using CFD–FSI (fluid-structure interaction), boundary-element acoustics and prototype measurements. These steps would determine whether the numerical ranking survives progressively more realistic descriptions without changing the present study from a transparent early-stage design model into an unsupported certification claim.

9. Conclusion

This paper presents an integrated interval type-2 fuzzy hydroelastic Ritz–Koopman model for robust vibro-acoustic suppression in a partially filled cylindrical tank. The mathematical model coupled Bessel sloshing modes, shell Ritz modes, nonlinear free-surface stiffness, acoustic radiation and fuzzy uncertainty propagation. A porous annular baffle and external viscoelastic-ring design was optimized using deterministic and fuzzy robust objectives. The proposed robust design reduced the 95th-percentile peak sound power from 57.840 dB to 48.548 dB and decreased the 95th-percentile band-averaged acoustic level from 28.466 dB to 26.726 dB. The method also reduced the 95th-percentile wall acceleration by 10.143 dB. The deterministic optimum had lower nominal, median and 95th-percentile peaks, whereas the proposed robust design provided a lower 95th-percentile band mean and wall-acceleration level. The narrowing alpha-plane intervals describe nested input cuts and are not evidence of physical uncertainty reduction. The study demonstrates that interval type-2 fuzzy modelling is a useful mathematical tool for sound-and-vibration systems where operating uncertainty is not adequately described by a single probability distribution.

Author contributions: Conceptualization, SIM and YN; methodology, SIM and YN; software, YN and PW; validation, SIM, SAB, PW and CNS; formal analysis, SIM and YN; investigation, SIM, YN and SAB; resources, SAB and AV; data curation, YN, PW and CNS; writing—original draft preparation, SIM and YN; writing—review and editing, SIM, YN, SAB, AV, PW and CNS; visualization, YN, PW and CNS; supervision, YN and AV; project administration, YN, SIM and AV. All authors have read and agreed to the published version of the manuscript.

Funding: No specific external funding is declared for this computational study.

Institutional review board statement: Not applicable.

Informed consent statement: Not applicable.

Data availability statement: All numerical datasets supporting the results are reported in the manuscript tables and figures. No supplementary files are required for reviewing the principal claims.

Conflicts of interest: The authors declare no conflict of interest.

AI use statement: During the preparation of this revised manuscript, the authors used ChatGPT (OpenAI) for language verification. The authors subsequently reviewed and edited the content as necessary and take full responsibility for the final content of the published article.

References

1. Housner GW. The dynamic behavior of water tanks. Bulletin of the Seismological Society of America. 1963; 53(2): 381–387. doi: 10.1785/BSSA0530020381
2. Gupta RK. Free vibrations of partially filled cylindrical tanks. Engineering Structures. 1995; 17(3): 221–230. doi: 10.1016/0141-0296(94)00004-D
3. Gonçalves PB, Ramos NRSS. Free vibration analysis of cylindrical tanks partially filled with liquid. Journal of Sound and Vibration. 1996; 195(3): 429–444. doi: 10.1006/jsvi.1996.0436
4. Amabili M, Païdoussis MP, Lakis AA. Vibrations of partially filled cylindrical tanks with ring-stiffeners and flexible bottom. Journal of Sound and Vibration. 1998; 213(2): 259–299. doi: 10.1006/jsvi.1997.1481

5. Askari E, Daneshmand F. Coupled vibration of a partially fluid-filled cylindrical container with a cylindrical internal body. Journal of Fluids and Structures. 2009; 25(2): 389–405. doi: 10.1016/j.jfluidstructs.2008.07.003
6. Askari E, Daneshmand F, Amabili M. Coupled vibrations of a partially fluid-filled cylindrical container with an internal body including the effect of free surface waves. Journal of Fluids and Structures. 2011; 27(7): 1049–1067. doi: 10.1016/j.jfluidstructs.2011.04.010
7. Ren K, Wu GX, Li ZF. Natural modes of liquid sloshing in a cylindrical container with an elastic cover. Journal of Sound and Vibration. 2021; 512: 116390. doi: 10.1016/j.jsv.2021.116390
8. Zhou D, Liu WQ. Hydroelastic vibrations of flexible rectangular tanks partially filled with liquid. International Journal for Numerical Methods in Engineering. 2007; 71(2): 149–174. doi: 10.1002/nme.1921
9. Chen YH, Hwang WS, Ko CH. Sloshing behaviours of rectangular and cylindrical liquid tanks subjected to harmonic and seismic excitations. Earthquake Engineering & Structural Dynamics. 2007; 36(12): 1701–1717. doi: 10.1002/eqe.713
10. Nezami M, Mohammadi MM, Oveisi A. Liquid sloshing in a horizontal circular container with eccentric tube under external excitation. Shock and Vibration. 2014; 2014(1): 507281. doi: 10.1155/2014/507281
11. Wang J, Liu J, Wang D. Coupled responses in a partially liquid-filled cylindrical tank with the single flexible baffle under pitching excitations. Shock and Vibration. 2019; 2019(1): 9854187. doi: 10.1155/2019/9854187
12. Wang J, Lo SH, Zhou D, et al. Nonlinear sloshing of liquid in a rigid cylindrical container with a rigid annular baffle under lateral excitation. Shock and Vibration. 2019; 2019(1): 5398038. doi: 10.1155/2019/5398038
13. Wang D, Lo SH, Zhou D. Liquid sloshing in rigid cylindrical container with multiple rigid annular baffles: free vibration. Journal of Fluids and Structures. 2012; 34: 138–156. doi: 10.1016/j.jfluidstructs.2012.06.006
14. Wang D, Lo SH, Zhou D. Sloshing of liquid in rigid cylindrical container with multiple rigid annular baffles: Lateral excitations. Journal of Fluids and Structures. 2013; 42: 421–436. doi: 10.1016/j.jfluidstructs.2013.07.005
15. Sharma V, Arun CO, Krishna IRP. Development and validation of a simple two degree of freedom model for predicting maximum fundamental sloshing mode wave height in a cylindrical tank. Journal of Sound and Vibration. 2019; 461: 114906. doi: 10.1016/j.jsv.2019.114906
16. Cao Z, Xue MA, Yuan X, et al. A fast semi-analytic solution of liquid sloshing in a 2-D tank with dual elastic vertical baffles and walls. Ocean Engineering. 2023; 273: 113951. doi: 10.1016/j.oceaneng.2023.113951
17. Ren Y, Xue MA, Lin P. Experimental study of sloshing characteristics in a rectangular tank with elastic baffles. Journal of Fluids and Structures. 2023; 122: 103984. doi: 10.1016/j.jfluidstructs.2023.103984
18. Liu D, Lu T, Qi C, et al. Influence of liquid viscosity on surface wave motion in a vertical cylindrical tank. Ocean Engineering. 2023; 289: 116192. doi: 10.1016/j.oceaneng.2023.116192
19. Moreau M, Kristiansen T, Ommani B, et al. Sloshing-induced motions of a spar inside a cylindrical dock with baffles in waves. Applied Ocean Research. 2023; 134: 103493. doi: 10.1016/j.apor.2023.103493
20. Liu X, Luo S, Luo S, et al. On the vibrational behavior of three-layered higher-order smart porous microplates with nanocomposite piezoelectric patches. Mechanics Based Design of Structures and Machines. 2024; 52(6): 3160–3181. doi: 10.1080/15397734.2023.2199058
21. Zhou Y, Zhang Y, Nyasha Chirukam B, et al. Free vibration analyses of stiffened functionally graded graphene-reinforced composite multilayer cylindrical panel. Mathematics. 2023; 11(17): 3662. doi: 10.3390/math11173662
22. Sahaj KV, Shri S, Nasar T. Sloshing dynamics in sway excited rectangular scaled tanks. Journal of Marine Science and Application. 2023; 22: 260–272. doi: 10.1007/s11804-023-00335-9
23. Şahin I, Ulu C. Online footprint of uncertainty tuning mechanism for single-input interval type-2 fuzzy PID controllers. International Journal of Fuzzy Systems. 2025. doi: 10.1007/s40815-025-02077-y
24. Storn R, Price K. Differential evolution: A simple and efficient heuristic for global optimization over continuous spaces. Journal of Global Optimization. 1997; 11: 341–359. doi: 10.1023/A:1008202821328
25. Hefny HA, Amer NS. Interval type-2 mutual subsethood Cauchy fuzzy neural inference system. International Journal of Computational Intelligence Systems. 2024; 17: 28. doi: 10.1007/s44196-024-00405-y
26. Chen M, Lam HK, Xiao B, et al. Stability analysis of interval type-2 sampled-data polynomial fuzzy-model-based control system with a switching control scheme. Nonlinear Dynamics. 2024; 112: 11111–11126. doi: 10.1007/s11071-024-09606-8
27. Sinha S, Nandanoori SP, Barajas-Solano DA. Online real-time learning of dynamical systems from noisy streaming data. Scientific Reports. 2023; 13: 22564. doi: 10.1038/s41598-023-49045-w
28. Colbrook MJ, Ayton LJ, Szőke M. Residual dynamic mode decomposition: Robust and verified Koopmanism. Journal of Fluid Mechanics. 2023; 955: A21. doi: 10.1017/jfm.2022.1052

29. Solera-Rico A, Sanmiguel Vila C, Gómez-López M, et al. β-variational autoencoders and transformers for reduced-order modelling of fluid flows. Nature Communications. 2024; 15: 1361. doi: 10.1038/s41467-024-45578-4
30. Fukami K, Murata T, Zhang K, et al. Sparse identification of nonlinear dynamics with low-dimensionalized flow representations. Journal of Fluid Mechanics. 2021; 926: A10. doi: 10.1017/jfm.2021.697